

BARD-GS: Blur-Aware Reconstruction of Dynamic Scenes via Gaussian Splatting

Yiren Lu, Yunlai Zhou, Disheng Liu, Tuo Liang, Yu Yin✉

Case Western Reserve University

{yiren.lu, yunlai.zhou, disheng.liu, tuo.liang, yu.yin}@case.edu

<https://vulab-ai.github.io/BARD-GS/>

Abstract

3D Gaussian Splatting (3DGS) has shown remarkable potential for static scene reconstruction, and recent advancements have extended its application to dynamic scenes. However, the quality of reconstructions depends heavily on high-quality input images and precise camera poses, which are not that trivial to fulfill in real-world scenarios. Capturing dynamic scenes with handheld monocular cameras, for instance, typically involves simultaneous movement of both the camera and objects within a single exposure. This combined motion frequently results in image blur that existing methods cannot adequately handle. To address these challenges, we introduce BARD-GS, a novel approach for robust dynamic scene reconstruction that effectively handles blurry inputs and imprecise camera poses. Our method comprises two main components: 1) camera motion deblurring and 2) object motion deblurring. By explicitly decomposing motion blur into camera motion blur and object motion blur and modeling them separately, we achieve significantly improved rendering results in dynamic regions. In addition, we collect a real-world motion blur dataset of dynamic scenes to evaluate our approach. Extensive experiments demonstrate that BARD-GS effectively reconstructs high-quality dynamic scenes under realistic conditions, significantly outperforming existing methods.

1. Introduction

The emergence of Neural Radiance Fields (NeRF) [32] and 3D Gaussian Splatting (3DGS) [16] has significantly advanced 3D scene reconstruction, with widespread applications in 3D editing [4, 11, 26, 44, 46, 55] and SLAM [15, 31, 36, 41, 64]. Recent research has extended NeRF and 3DGS to dynamic scenes [1, 9, 27, 53, 54, 63], demonstrating promising results. However, their performance declines when processing motion-blurred images.

Motion blur is a common occurrence in everyday pho-

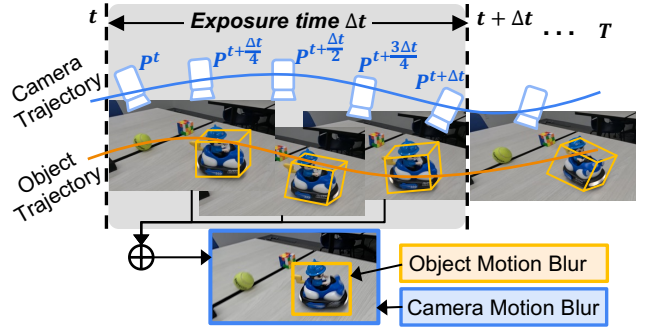


Figure 1. **The formation process of motion blur.** It originates from two sources: camera-induced blur caused by camera movements during exposure, and object-induced blur resulting from fast objects moving. The static regions of a scene are affected solely by camera motion blur, while dynamic regions are impacted by both camera and object motion blur.

tography, typically arising from movements during the exposure time, as demonstrated in Fig. 1. It can be decomposed as camera- and object-induced blur. Beyond the loss of visual clarity, motion blur introduces geometric inconsistencies across frames, posing a significant challenge to existing 3D reconstruction methods. While prior works have explored motion-blurred reconstruction [22, 29, 47, 50, 61], they primarily focus on static scenes, lacking the ability to handle dynamic object motion. Moreover, integrating existing deblur-GS [50, 61] with dynamic-GS frameworks [53, 54] addresses only camera-induced blur, leaving object motion blur unresolved.

There are two NeRF-based approaches [3, 42] trying to eliminate both types of motion blur by optimizing multiple latent rays across exposure time and warping them at different timestamps for dynamic rendering. However, these methods couple object and camera motion effects within the latent ray representation. Since static region typically dominates the scene, rays tend to adjust primarily for camera motion blur, resulting in poor reconstruction in dynamic areas, especially with severe blur caused by fast-moving objects.

Besides, the implicit neural representation of NeRF makes it challenging to decouple these effects.

In this paper, we present **BARD-GS**, a **Blur-Aware Reconstruction** framework for **Dynamic** scenes based on **Gaussian Splatting**. To tackle the challenges posed by blurry input, we decompose motion blur into two types: *camera motion blur*, modeled by variations in camera pose, and *object motion blur*, modeled by the movement of dynamic Gaussians. By modeling these two types of blur separately, we address the problem in two sequential stages: 1) camera motion deblurring and 2) object motion deblurring.

In the first stage, we address camera motion blur by modeling the camera’s trajectory within each exposure time as a sequence of virtual camera poses. We simulate camera motion blur by rendering images from these virtual poses and combining them to reconstruct blurry images. By aligning the static regions of reconstructed blurry images to the input images, we optimize the 3D Gaussians to sharply reconstruct the static regions of the scene, effectively isolating and eliminating camera-induced blur. Note that this stage focuses exclusively on static regions to better distinguish camera and object motion blur.

In the second stage, we address object motion blur and accurately reconstruct dynamic regions while further refining static areas. We learn a time-conditioned deformation field to track the spatial shifts of 3D Gaussians over time, capturing the motion of dynamic objects. Similar to camera movement modeling, we model the object positions at different timestamps within the exposure time, using the trajectory of 3D Gaussians. We then render images of dynamic objects at virtual timestamps and combine rendered images to reconstruct object-induced blur. By aligning the entire reconstructed blurry images with the input, we achieve sharp reconstructions for both dynamic and static areas. This explicit separation and modeling of camera- and object-induced blur greatly enhance the rendering quality in dynamic regions compared to previous approaches.

In the absence of existing dynamic scene datasets with motion blur, we collect a real-world dataset to address this gap. Different from synthetic datasets used in previous works, where blurry images are generated by averaging consecutive frames, our dataset captures motion blur that closely aligns with real-world scenarios. We provide paired blurry and sharp images captured from diverse environments; details about the dataset acquisition can be found in Sec. 4.1. In summary, our key contributions include:

- We propose BARD-GS, a blur-aware dynamic scene reconstruction framework, to tackle challenges posed by blurry inputs and imprecise camera poses.
- We decouple object motion blur from camera motion blur and model each separately in an explicit manner, resulting in a substantial improvement in reconstruction quality within dynamic regions compared to previous methods.

- A new real-world motion blur dataset is proposed for evaluating the novel view synthesis performance under real-world blurry scenarios.

2. Related Work

2.1. Image Deblurring

The primary objective of image deblurring is to recover a clear image from a blurry one. Recently, due to the power of deep learning, image deblurring tasks have mainly focused on learning-based methods to solve the problem. In single-image deblurring, existing methods primarily achieve deblurring by leveraging CNN-based models [59], Transformer-based models [57] or by reconstructing the image with the help of prior knowledge from generative models [19]. With the rapid development of deep learning, these works [5, 18, 19, 43, 57, 59] have achieved superior result on single image deblurring. Although these methods achieve impressive results, they primarily work within the 2D image space and are unable to capture scene geometry in 3D space, leading to limitations in maintaining spatial consistency. Our method achieves deblurring in dynamic 3D scenes by physically modeling the blur formation process, demonstrating a better result compared to 3D reconstruction with pre-deblurred images.

2.2. Dynamic 3D Gaussian Splatting

3D Gaussian Splatting (3DGS) [16] has been a popular 3D scene representation, known for its explicit structure and real-time novel view rendering. As originally designed for static scenes, 3DGS lacks capability for dynamic scene modeling. Recently, various researches [1, 9, 13, 17, 24, 27, 48, 53, 54, 63] have attempted to adapt it for dynamic scene reconstruction. In order to model the dynamic scene, Dynamic 3D Gaussians [28] utilize a table to store the information of each 3D Gaussians at every timestamp, including mean and variance of Gaussians. 4D Gaussian Splatting [54] achieves dynamic scene modeling by directly lifting the original 3D Gaussian into 4D space. Deformable-3D-Gaussians [53] utilize a multi-layer perceptron (MLP) to learn the position, rotation, and scale for each 3D Gaussians at every timestamp. These methods have achieved excellent dynamic scene reconstruction results, however, all of them require high-quality sharp images and precise camera poses as input. Our approach considers the physical process of motion blur formation, enabling it to handle inputs with both camera-induced and object-induced motion blur, resulting in substantially improved reconstruction quality.

2.3. 3D Reconstruction from Blurry Input

Recently, there have been many NeRF-based [21, 29, 34, 47] and 3DGS-based [6, 20, 23, 35, 39, 50, 61] methods trying to achieve high-quality 3D reconstruction from blurry

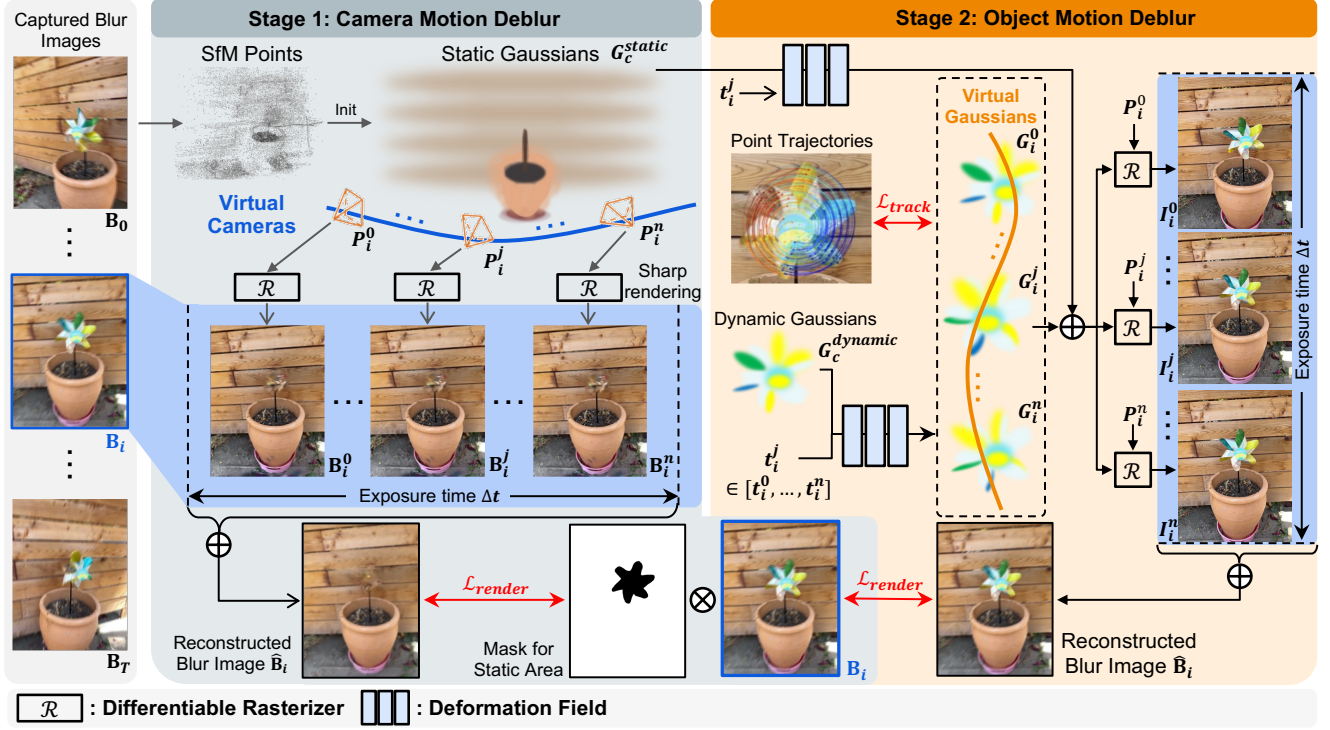


Figure 2. **An overview of the pipeline.** Our method consists of two stages: camera motion deblur and object motion deblur. In the first stage, we handle camera motion blur by modeling the camera’s trajectory during each exposure, resulting in sharp reconstruction in the static regions. Then, we utilized the optimized camera poses together with the depth map obtain from DepthAnything to initialize the dynamic Gaussians. In the second stage, we address object motion blur by modeling the trajectory of 3D Gaussians within each exposure using deformation field, which allow us to achieve clear reconstruction in the dynamic regions.

input. Deblur-NeRF [29] utilizes a Deformable Sparse Kernel (DSK) to model the formation of blur by deforming the canonical kernel. BAD-NeRF [47], BAD-Gaussians [61] and Deblur-GS [50] model the camera trajectory during the exposure time, generating multiple sharp images along the path and blending them to simulate the process of blur formation. These methods can produce high-quality rendering results for static scenes, however, none of them is designed to handle dynamic scenes. There are two works share the same goal with us [3, 42] and both of them are NeRF-based. They share a same idea to generate multiple latent rays within the exposure time to model the blur formation process. The rays are then twisted to perform volume rendering on different points across various timestamps, allowing for dynamic modeling. In this approach, the blurring effects from both camera and object motion are combined within a single ray warping process, causing them to be interdependent. As a result, the static regions dominate, leading to poor detail representation in dynamic areas. Our method explicitly decouples these two sources of blur by modeling the motion of camera and the motion of dynamic Gaussians. By handling them sequentially, our method achieves significantly improved rendering results in dynamic regions.

3. Method

We introduce BARD-GS, a blur-aware dynamic scene reconstruction method based on Gaussian Splatting, designed to reconstruct scenes from blurry input. Our approach explicitly separates motion blur into two components: *camera motion blur* and *object motion blur*. These are modeled independently using the trajectories of cameras and 3D Gaussians, respectively. In Sec. 3.1 and 3.2, we provide an overview of 3DGS and the formation of motion blur, respectively. We then describe the two main components of our pipeline: 1) camera motion deblurring (Sec. 3.3) and 2) object motion deblurring (Sec. 3.4), illustrating how each type of blur is effectively addressed.

3.1. Preliminary: 3D Gaussian Splatting

3D Gaussian Splatting (3DGS) [16] represents a scene using 3D Gaussian ellipsoids, each parameterized by a center \mathbf{x} , covariance matrix Σ , opacity α and learnable spherical harmonics for color. During differentiable rasterization, 3D Gaussians are first projected into 2D image space with a given camera pose. Then each pixel color $\hat{c}(\mathbf{x})$ is calculated based on the overlapping Gaussians projected onto it, using

the alpha-blending process:

$$\hat{c}(\mathbf{x}) = \sum_{i \in \mathcal{N}} c_i \alpha_i(\mathbf{x}) \prod_{j=1}^{i-1} (1 - \alpha_j(\mathbf{x})), \quad (1)$$

where c_i is the color of each projected Gaussian given by spherical harmonics and α_i is the opacity multiplies with the projected covariance matrix Σ' . During reconstruction, the parameters of 3D Gaussians are optimized by minimizing the pixel-wise L1 loss together with SSIM loss between the rendered image \hat{I} and the ground truth image I_{gt} .

3.2. Motion Blur Formation

Motion blur results from the movement of cameras or object within an exposure time. In the perspective of physics, due to the above-mentioned movement, the photons from a single object will accumulate across different locations on the sensor, resulting in a “trail” or streaked path that corresponds to the motion trajectory. The physical process can be described by the following equation:

$$\mathbf{B}(\mathbf{u}, \mathbf{v}) = \phi \int_0^\tau \mathbf{S}_t(\mathbf{u}, \mathbf{v}) dt, \quad (2)$$

where $\mathbf{S}_t(\mathbf{u}, \mathbf{v})$ is the instantaneous radiance of the scene at pixel location (\mathbf{u}, \mathbf{v}) at a specific time t within an exposure time τ . $\mathbf{B}(\mathbf{u}, \mathbf{v})$ is the resulting blurred pixel at (\mathbf{u}, \mathbf{v}) , calculated by integrating instantaneous radiance over an exposure duration, “averaging” the positions of objects in motion, and ϕ is a normalization factor. To facilitate the simulation of this process, we utilize a discretized version of the above equation:

$$\mathbf{B}(\mathbf{u}, \mathbf{v}) \approx \frac{1}{n} \sum_{i=0}^{n-1} \mathbf{S}_i(\mathbf{u}, \mathbf{v}). \quad (3)$$

Here, the blurry image \mathbf{B} is approximated by averaging n discrete sharp images \mathbf{S}_i captured within an exposure time.

3.3. Camera Motion Modeling and Deblurring

In camera motion deblurring, we will handle motion blur caused by camera movement and reconstruct static part of the scene. Inspired by [61], we compute a set of corresponding virtual camera poses for each real camera to represent the camera movement within an exposure time. Here, we refer to the camera associated with each input image as a *real camera*, and the cameras interpolated within the exposure time as *virtual cameras*. These virtual cameras are used to render virtual sharp images, which will be averaged to reconstruct the blurry input.

3.3.1. Camera Optimization and Trajectory Modeling

Given a set of T blurry images $\{\mathbf{B}_i\}_{i=1}^T$ as input, we utilize off-the-shelf SfM method COLMAP [37, 38] to get initial inaccurate camera poses $\{\tilde{\mathbf{P}}_i\}_{i=1}^T$. For each real camera

pose $\tilde{\mathbf{P}}_i$, the corresponding set of virtual cameras is denoted as $\{\mathbf{P}_i^j\}_{j=0}^n$, \mathbf{P}_i^j represents the j th virtual camera associate with the i th blurry image. Each \mathbf{P}_i^j consists of \mathbf{R}_i^j and \mathbf{t}_i^j , representing rotation and translation. These virtual cameras are interpolated from \mathbf{P}_i^0 and \mathbf{P}_i^n , which represent the poses at the beginning and the end of the exposure period. \mathbf{P}_i^0 and \mathbf{P}_i^n are calculated by applying a learnable delta value to the inaccurate pose $\tilde{\mathbf{P}}_i$.

$$\mathbf{P}_i^0 = \tilde{\mathbf{P}}_i \cdot \Delta \mathbf{P}_i^0, \quad \mathbf{P}_i^n = \tilde{\mathbf{P}}_i \cdot \Delta \mathbf{P}_i^n \quad (4)$$

The intermediate poses $\{\mathbf{P}_i^j\}_{j=1}^{n-1}$ are calculated through linear interpolation, note that the interpolation of rotation is calculated on the $\mathfrak{so}(3)$ manifold [40], implemented using PyPose [45, 58]. The interpolation process is described as the following equations:

$$\mathbf{R}_i^j = \mathbf{R}_i^0 \cdot \exp\left(\frac{j}{n} \cdot \log((\mathbf{R}_i^0)^{-1} \cdot \mathbf{R}_i^n)\right), \quad (5)$$

$$\mathbf{t}_i^j = \mathbf{t}_i^0 + \frac{j}{n} \cdot (\mathbf{t}_i^n - \mathbf{t}_i^0), \quad (6)$$

where $\exp(\cdot)$ and $\log(\cdot)$ represents the exponential mapping and logarithmic mapping between $\mathbf{SO}(3)$ and $\mathfrak{so}(3)$. During the evaluation process, we utilize the mid-point interpolation between \mathbf{P}_i^0 and \mathbf{P}_i^n , denoted as \mathbf{P}_i^{mid} to serve as the optimized camera poses for rendering.

3.3.2. Camera Motion Deblurring

Provided with the set of virtual cameras, the corresponding blurry image can be synthesized as follows:

$$\hat{\mathbf{B}}_i = \frac{1}{n+1} \sum_{j=0}^n \mathbf{I}_i^j(\mathbf{P}_i^j, \mathbf{G}_c^{static}), \quad (7)$$

where $\mathbf{I}_i^j(\mathbf{P}_i^j, \mathbf{G}_c^{static})$ denotes the virtual sharp image rendered with virtual pose \mathbf{P}_i^j and the canonical space static Gaussians \mathbf{G}_c^{static} , $\hat{\mathbf{B}}_i$ is the reconstructed blurry image.

The loss function for learning virtual cameras as well as reconstructing the static region is a rendering loss between input blurry image \mathbf{B}_i and reconstructed blurry image $\hat{\mathbf{B}}_i$:

$$\mathcal{L}_{render} = \sum_{(x,y) \notin M_d} \|\hat{\mathbf{B}}_i(x,y) - \mathbf{B}_i(x,y)\|_1, \quad (8)$$

where M_d is a dynamic mask obtained from Track-Anything [51], as we do not want the content within the dynamic region to affect the optimization of camera poses.

3.4. Object Motion Modeling and Deblurring

After the camera motion deblurring stage, we removed the blurry effect caused by camera movement and reconstructed a sharp static region of the scene. In this section, we will dive into details on how we model object motion and apply object motion deblurring.

3.4.1. Object Motion Modeling

To model object motion, we utilize a multi-layer perceptron (MLP) to serve as a deformation field:

$$(\delta \mathbf{x}, \delta \mathbf{r}, \delta \mathbf{s}) = \mathcal{F}_\theta(\gamma(\mathbf{x}), \gamma(t)), \quad (9)$$

where \mathcal{F}_θ represents deformation field, $\gamma(\cdot)$ denotes positional encoding, \mathbf{x} denotes the canonical space mean of the input dynamic Gaussian, t is the input timestamp and $(\delta \mathbf{x}, \delta \mathbf{r}, \delta \mathbf{s})$ is the output offsets to transform canonical space Gaussians into the deformed space at time t .

Besides, to further refine the details in the static region, we introduce an extra deformation field to the static Gaussians. It can handle the byproducts resulting from the moving objects (e.g. reflection and shadow) and improve the poor rendering quality in the marginal area due to the lack of initial Gaussians. In the following section, we denote the static deformation field and dynamic deformation field together as \mathcal{F}_θ , for ease of understanding.

3.4.2. Object Motion Deblurring

Similar to camera motion deblurring in Sec. 3.3, object motion deblurring is achieved by finding a set of virtual times $\{t_i^j\}_{j=0}^n$, where t_i^j denotes the j th virtual timestamp around t_i , the corresponding timestamp of the blurry input \mathbf{B}_i . With these virtual times, we can query the deformation field to obtain the trajectories of Gaussians \mathbf{G}_i^j (i.e. virtual Gaussians) that represent the moving objects, where $\mathbf{G}_i^j = \mathbf{G}_c + \mathcal{F}_\theta(\gamma(\mathbf{X}), \gamma(t_i^j))$, in which \mathbf{X} denotes the mean of the canonical space Gaussians, \mathbf{G}_c is the canonical space Gaussians consists of \mathbf{G}_c^{static} and \mathbf{G}_c^{dyn} . Notice that the number of virtual times should equal the number of virtual views. Thus, we can update Eq. 7 to the following:

$$\hat{\mathbf{B}}_i = \frac{1}{n+1} \sum_{j=0}^n \mathbf{I}_i^j(\mathbf{P}_i^j, \mathbf{G}_i^j), \quad (10)$$

where $\mathbf{I}_i^j(\mathbf{P}_i^j, \mathbf{G}_i^j)$ is the virtual sharp image rendered with virtual camera pose \mathbf{P}_i^j and the Gaussians \mathbf{G}_i^j at virtual time t_i^j . We make an assumption that objects move at a constant speed within the exposure time, thus $\{t_i^j\}_{j=0}^n$ are interpolated uniformly in $[t_i - \frac{\tau}{2}, t_i + \frac{\tau}{2}]$, where τ denotes one exposure time. The training objective in this part is still the rendering loss, but considering the entire image:

$$\mathcal{L}_{render} = \sum_{(x,y) \in \mathbf{B}_i} \|\hat{\mathbf{B}}_i(x,y) - \mathbf{B}_i(x,y)\|_1. \quad (11)$$

3.4.3. Trajectory of Gaussians

In the Subsec. 3.4.2, we implicitly assume the deformation field will learn the actual trajectory of each Gaussian. However, due to the implicit nature of the deformation field, we cannot constrain what Gaussian movements it will learn.



Figure 3. **Demonstration of artifacts in synthesized dataset.**

According to our experiments, in most cases, Gaussians will not follow the movement of the objects, which means a single moving object will be represented by different groups of Gaussians at different times. Thus it cannot fulfill our hypothesis. To solve this issue, we introduce a 3D track loss to constrain the movement of the Gaussians at the initial stage of training, forcing them to follow the motion of 2D pixels:

$$\mathcal{L}_{track} = \sum_{\mathbf{x}_i \in dynamic} \|\mathbf{x}_i^{gt} - \mathbf{x}_i\|_1, \quad (12)$$

where \mathbf{x}_i is the learned dynamic Gaussian means produced by deformation field at time i , which is the time corresponds to the blurry input \mathbf{B}_i , and \mathbf{x}_i^{gt} is the reference for dynamic Gaussian means. We first utilize BootsTAPIR [7, 8] to get a reference trajectory for each 2D pixel within the dynamic mask M_d . Next, we apply Depth-Anything [52] to obtain depth information. Then we utilize the optimized camera poses given in Sec. 3.3.1 to backproject the 2D pixel trajectories into 3D space to form pseudo ground truth for 3D Gaussian trajectories $\{\mathbf{x}_i^{gt}\}_{i=1}^T$. 3D track loss not only encourages deformation field to learn the actual trajectories, it also helps model fast object motion better.

4. Dataset

4.1. Synthesized Blurry Dataset

We generate a synthesized blurry dataset by following instructions in [3] to create blurred images from clean scene images. Utilizing the pre-trained Video Frame Interpolation (VFI) model, RIFE [12], we first increase the frame rate of the original input (e.g., from 30fps to 240fps). These interpolated sharp frames are then averaged to simulate the blur formation process, resulting in blurred images. This synthesized blurry dataset is used for deblurring evaluation.

For this task, we select three scenes from the HyperNeRF dataset [33] and four scenes from the Dycheck dataset [10], containing either relatively fast camera or object motion, to assess the effectiveness of our proposed method.

4.2. Real-world Captured Blurry Dataset

Though there exist several real-world blurry datasets [25, 29] for 3D reconstruction, they lack dynamic objects in

Table 1. **Quantitative comparison of deblurring**, conducted on synthesized blurry dataset. Colors indicate the **best** and **second best** results respectively. LV denotes Laplacian Variance.

Methods	Deblurring				
	PSNR \uparrow	SSIM \uparrow	LPIPS \downarrow	LV \uparrow	MUSIQ \uparrow
DyBluRF [42]	23.82	0.6900	0.4714	10.73	32.95
D3DGS [53]	27.20	0.7986	0.3486	20.62	37.74
D3DGS + [56]	27.98	0.8372	0.3289	36.34	52.16
4DGS [54]	27.39	0.8010	0.3399	18.48	39.14
4DGS + [56]	28.17	0.8335	0.2641	47.74	54.00
Ours	28.75	0.8414	0.2343	65.31	57.03

Table 2. **Quantitative comparison on real-world captured dataset**. When facing highly blurred images in our dataset, MPRNet fails to restore the sharp images. The experiment demonstrates our better performance compared with the baseline methods, including the pre-deblurred ones. LV denotes Laplacian Variance, and SI-* denotes shift-invariant metrics.

Methods	Novel View Synthesis				
	SI-PSNR \uparrow	SI-SSIM \uparrow	SI-LPIPS \downarrow	LV \uparrow	MUSIQ \uparrow
DyBluRF [42]	20.57	0.7614	0.3614	35.16	31.05
D3DGS [53]	22.83	0.8243	0.3500	18.95	28.89
D3DGS + [56]	23.10	0.8363	0.2637	37.58	38.73
4DGS [54]	22.06	0.8093	0.3733	24.60	30.17
4DGS + [56]	22.58	0.8293	0.2863	50.68	41.88
Ours	25.13	0.8508	0.1567	96.42	54.29

the scene for evaluating the performance of dynamic reconstruction. Previous works [3, 42] utilize clean datasets to synthesize blurry datasets to evaluate the performance of their models. However, blurry data synthesized in this way (*i.e.* Sec. 4.1) is often insufficiently blurred and may have some unrealistic artifacts, *i.e.* moiré pattern and consecutive edges, as shown in Fig. 3. Also, due to the short exposure time and fast shutter speed of the camera, all the sharp frames were captured under good lighting conditions, which is not realistic for motion blurs to occur.

To solve the problem of lacking blurry dynamic scene data, we collect a real-world blurry dataset for dynamic reconstruction. Our dataset contains 12 scenes, each of which is captured with two GoPros. We set one of the GoPros to 1/24 second exposure time to capture motion blurred images for training and the other one is set to 1/240 second exposure time to capture sharp images for evaluation. The two GoPros are synchronized using timecode. We use this real-world blurry dataset to evaluate novel view synthesis.

5. Experiments

5.1. Implementation Details

Our method is trained for 80,000 iterations. For the first 10,000 iterations, we use Eq. 8 as the loss function to optimize virtual cameras as well as reconstruct the static region. Then for iteration 10,000 to 30,000, we introduce a static deformation field and use Eq. 11 as the rendering loss, together with Eq. 12 forcing the deformation field to learn

from 2D pixel movements. Since we assume one-to-one correspondence between Gaussians and 3D track points, the splitting, duplicating and culling for dynamic Gaussians is temporarily suspended in this stage. For the rest of the training process, we remove Eq. 12 and rely solely on Eq. 11 as the loss function, while resuming splitting, duplicating, and culling of dynamic Gaussians.

5.2. Baselines and Evaluation Metrics

Baselines. We compare our method with DyBluRF [42], which is designed for dynamic reconstruction with motion blur and state-of-the-art dynamic reconstruction methods D3DGS [53] and 4DGAussians [54] as well. Since D3DGS and 4DGAussians lack deblurring capabilities, we also pre-process the training images using the pre-trained deblurring method MPRNet [56] to evaluate the performance.

Evaluation Metrics. In addition to commonly used metrics like PSNR, SSIM, and LPIPS, we incorporate additional metrics to further showcase our rendering quality. Our experiments show that PSNR can sometimes yield higher values even when images appear blurrier. Therefore, we introduce Laplacian Variance (LV) and MUSIQ [14] to better assess the sharpness and the overall quality of the rendered images. For Novel View Synthesis, we extract training poses and evaluation poses from blurry images and sharp images respectively. However, it is quite challenging to align these two sets of poses to the same local coordinate system perfectly, which will lead to a slight shift in the rendered image. Thus, we utilize shift-invariant metrics in Tab. 2 for quantitative comparisons. For the shift-invariant metrics, we allow a 6-pixel shift in both horizontal and vertical axes, and choose the largest value among the 36 results.

5.3. Deblurring

For the deblurring task, we evaluate our method against baseline methods using synthesized datasets generated from both Dycheck [10] and HyperNeRF [33]. The blurred images serve as input, and the original sharp images are used for evaluation. Our quantitative comparison results are presented in Tab. 1. The results show that our method outperforms all baselines. The significant performance gap in LPIPS, LV, and MUSIQ scores indicate that DyBluRF, D3DGS, and 4DGS are suffering from motion-blurred inputs. Qualitative results are provided in Fig. 4. Our method provides superior visual results in both static and dynamic regions. Notably, in the last row, our rendering results appear even clearer than the ground truth. This is because the ground truth images in the Dycheck dataset were captured at a low frame rate, resulting in some blurring.

5.4. Novel View Synthesis

For the novel view synthesis task, we compare our method with baseline approaches on our real-world blurry dataset,

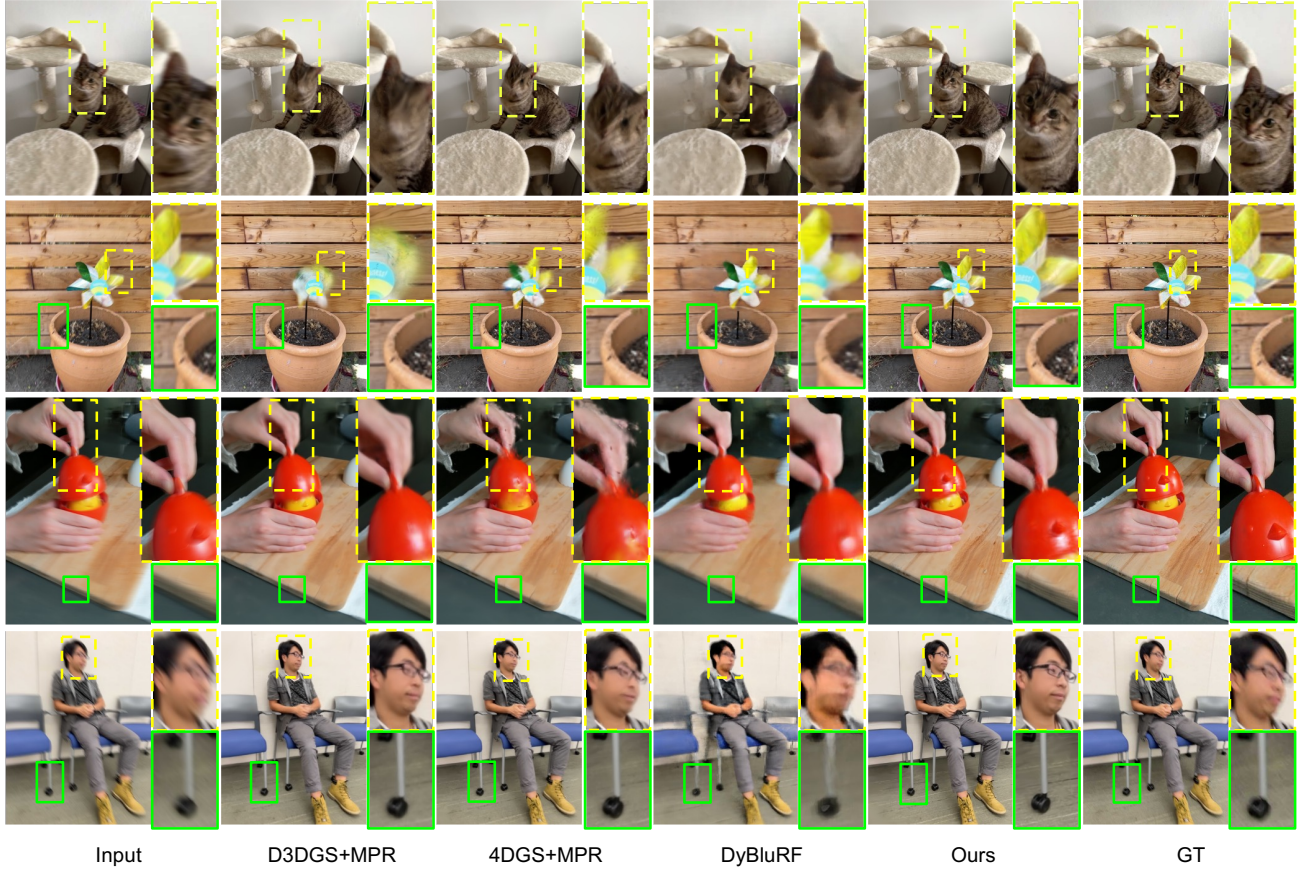


Figure 4. **Qualitative comparison of deblurring.** The green boxes represent details in static region and the dashed yellow boxes denote the dynamic part. As Dycheck dataset is not captured at high frame rate, our method produces a better result than GT in the last row.

Table 3. **Ablation studies on each module of our proposed method.** TL: Track Loss, DB: Dynamic Deblurring, SD: Static Deblurring, SDF: Static Deformation Field. LV denotes Laplacian Variance, and SI-* denotes shift-invariant metrics.

	Deblurring					Novel View Synthesis				
	PSNR \uparrow	SSIM \uparrow	LPIPS \downarrow	LV \uparrow	MUSIQ \uparrow	SI-PSNR \uparrow	SI-SSIM \uparrow	SI-LPIPS \downarrow	LV \uparrow	MUSIQ \uparrow
w/o TL	27.68	0.8186	0.2757	57.53	54.69	24.12	0.8272	0.1993	88.24	50.35
w/o DB	28.47	0.8229	0.2614	59.31	55.59	24.11	0.8229	0.1873	91.76	51.87
w/o SD	26.00	0.7514	0.3743	16.42	36.57	22.22	0.7656	0.2702	24.69	29.51
w/o SDF	27.19	0.8057	0.2814	59.42	52.37	24.40	0.8244	0.2534	76.58	44.05
Ours	28.75	0.8414	0.2343	65.31	57.03	25.13	0.8508	0.1567	96.42	54.29

Table 4. **Ablation studies on the number of virtual views.** Each color indicates the best, second best and third best respectively. The results indicate that increasing virtual cameras enhances model performance but peaks at a certain point.

# virtual views	toycar			windmill		
	SI-PSNR \uparrow	SI-SSIM \uparrow	SI-LPIPS \downarrow	SI-PSNR \uparrow	SI-SSIM \uparrow	SI-LPIPS \downarrow
6	23.45	0.8660	0.1557	26.74	0.9034	0.1421
8	23.63	0.8665	0.1546	26.75	0.9028	0.1424
10	23.47	0.8676	0.1419	27.52	0.9063	0.1275
15	22.96	0.8532	0.1667	26.83	0.9062	0.1376
20	23.33	0.8625	0.1589	26.31	0.8977	0.1388

as stated in Sec. 5.2. The quantitative results are shown in Tab. 2. When facing highly blurred images in our dataset, MPRNet fails to restore the sharp images. Our method delivers superior results across all aspects, with a wider performance gap compared to the deblurring task. We also provide a qualitative comparison in Fig. 5. Our method demonstrates significantly better rendering quality within dynamic regions while preserving fine details in static areas.

5.5. Ablation Study

Component ablation. We first conduct ablation studies to evaluate the contributions of each component in our proposed method on both deblurring and novel view synthe-



Figure 5. **Qualitative comparison of Novel View Synthesis.** Our method shows a significantly better rendering quality in the dynamic region, *e.g.* the windmill, the face details, card and the toy car. Besides, for static region, our method reconstructs finer details and shows a even better result than the ground truth image, *e.g.* the details in the green bounding box in the second column.

sis tasks. We evaluate the impact of (1) removing tracking loss (w/o TL), (2) removing dynamic deblurring (w/o DB), (3) removing static deblurring (w/o SD) and (4) removing static deformation field (w/o SDF). The quantitative results are shown in Tab. 3. We can observe a huge performance degradation without static deblurring, which is reasonable, since static region dominates the scene. Removing either tracking loss or dynamic deblurring will result in a lower rendering quality. One thing to be noticed is that removing dynamic deblurring in the deblurring task has less impact because the scenes in the synthesized dataset generally have less blurry effect than the real-world blurry dataset.

Virtual camera poses. We also conduct experiments to show the effect of the number of virtual views within the exposure time, as described in Sec. 3.3. We choose a set of numbers ranging from 6 to 20, representing the number of virtual views, and randomly pick two scenes (*i.e.* toy car

and windmill) to conduct this ablation study. The quantitative results are shown in Tab. 4. Our results indicate that increasing the number of virtual views will help improves motion blur handling up to a certain point, after which additional views become counterproductive.

6. Conclusion

We introduce BARD-GS, a Gaussian Splatting-based method for dynamic scene reconstruction from blurry inputs. By explicitly decoupling and modeling both object and camera motion blur, our approach achieves superior reconstruction quality compared to previous methods. In addition, we present a real-world blurry dataset for dynamic scene reconstruction, which will be released to benefit further research in the community.

References

- [1] Jeongmin Bae, Seoha Kim, Youngsik Yun, Hahyun Lee, Gun Bang, and Youngjung Uh. Per-gaussian embedding-based deformation for deformable 3d gaussian splatting. In *European Conference on Computer Vision (ECCV)*, 2024. 1, 2
- [2] Raghav Bansal, Gaurav Raj, and Tanupriya Choudhury. Blur image detection using laplacian operator and open-cv. In *2016 International Conference System Modeling & Advancement in Research Trends (SMART)*, pages 63–67. IEEE, 2016. 2
- [3] Minh-Quan Viet Bui, Jongmin Park, Jihyong Oh, and Munchurl Kim. Dyblurf: Dynamic deblurring neural radiance fields for blurry monocular video. *arXiv preprint arXiv:2312.13528*, 2023. 1, 3, 5, 6
- [4] Yiwen Chen, Zilong Chen, Chi Zhang, Feng Wang, Xiaofeng Yang, Yikai Wang, Zhongang Cai, Lei Yang, Huaping Liu, and Guosheng Lin. Gaussianeditor: Swift and controllable 3d editing with gaussian splatting. In *Proceedings of the IEEE/CVF conference on computer vision and pattern recognition*, pages 21476–21485, 2024. 1
- [5] Zheng Chen, Yulun Zhang, Ding Liu, Jinjin Gu, Linghe Kong, Xin Yuan, et al. Hierarchical integration diffusion model for realistic image deblurring. *Advances in neural information processing systems*, 36, 2024. 2
- [6] François Darmon, Lorenzo Porzi, Samuel Rota-Bulò, and Peter Kotschieder. Robust gaussian splatting. *arXiv preprint arXiv:2404.04211*, 2024. 2
- [7] Carl Doersch, Yi Yang, Mel Vecerik, Dilara Gokay, Ankush Gupta, Yusuf Aytar, Joao Carreira, and Andrew Zisserman. TAPIR: Tracking any point with per-frame initialization and temporal refinement. In *Proceedings of the IEEE/CVF International Conference on Computer Vision*, pages 10061–10072, 2023. 5
- [8] Carl Doersch, Pauline Luc, Yi Yang, Dilara Gokay, Skanda Koppula, Ankush Gupta, Joseph Heyward, Ignacio Rocco, Ross Goroshin, João Carreira, and Andrew Zisserman. Boot-sTAP: Bootstrapped training for tracking-any-point. *Asian Conference on Computer Vision*, 2024. 5
- [9] Yuanxing Duan, Fangyin Wei, Qiyu Dai, Yuhang He, Wenzheng Chen, and Baoquan Chen. 4d-rotor gaussian splatting: towards efficient novel view synthesis for dynamic scenes. In *ACM SIGGRAPH 2024 Conference Papers*, pages 1–11, 2024. 1, 2
- [10] Hang Gao, Ruilong Li, Shubham Tulsiani, Bryan Russell, and Angjoo Kanazawa. Dynamic novel-view synthesis: A reality check. In *NeurIPS*, 2022. 5, 6, 1, 2
- [11] Ayaan Haque, Matthew Tancik, Alexei A Efros, Aleksander Holynski, and Angjoo Kanazawa. Instruct-nerf2nerf: Editing 3d scenes with instructions. In *Proceedings of the IEEE/CVF International Conference on Computer Vision*, pages 19740–19750, 2023. 1
- [12] Zhewei Huang, Tianyuan Zhang, Wen Heng, Boxin Shi, and Shuchang Zhou. Real-time intermediate flow estimation for video frame interpolation. In *Proceedings of the European Conference on Computer Vision (ECCV)*, 2022. 5
- [13] Kai Katsumata, Duc Minh Vo, and Hideki Nakayama. A compact dynamic 3d gaussian representation for real-time dynamic view synthesis. In *European Conference on Computer Vision*, pages 394–412. Springer, 2024. 2
- [14] Junjie Ke, Qifei Wang, Yilin Wang, Peyman Milanfar, and Feng Yang. Musiq: Multi-scale image quality transformer. In *Proceedings of the IEEE/CVF international conference on computer vision*, pages 5148–5157, 2021. 6, 2
- [15] Nikhil Keetha, Jay Karhade, Krishna Murthy Jatavallabhula, Gengshan Yang, Sebastian Scherer, Deva Ramanan, and Jonathon Luiten. Splatam: Splat, track & map 3d gaussians for dense rgb-d slam. In *Proceedings of the IEEE/CVF Conference on Computer Vision and Pattern Recognition*, 2024. 1
- [16] Bernhard Kerbl, Georgios Kopanas, Thomas Leimkühler, and George Drettakis. 3d gaussian splatting for real-time radiance field rendering. *ACM Transactions on Graphics*, 42 (4), 2023. 1, 2, 3
- [17] Agelos Kratimenos, Jiahui Lei, and Kostas Daniilidis. Dynmf: Neural motion factorization for real-time dynamic view synthesis with 3d gaussian splatting. In *European Conference on Computer Vision*, pages 252–269. Springer, 2024. 2
- [18] Orest Kupyn, Volodymyr Budzan, Mykola Mykhailych, Dmytro Mishkin, and Jiří Matas. Deblurgan: Blind motion deblurring using conditional adversarial networks. In *Proceedings of the IEEE/CVF Conference on Computer Vision and Pattern Recognition (CVPR)*, pages 8183–8192, 2018. 2
- [19] Orest Kupyn, Tetiana Martyniuk, Junru Wu, and Zhangyang Wang. Deblurgan-v2: Deblurring (orders-of-magnitude) faster and better. In *Proceedings of the IEEE/CVF International Conference on Computer Vision (ICCV)*, pages 8878–8887, 2019. 2
- [20] Byeonghyeon Lee, Howoong Lee, Xiangyu Sun, Usman Ali, and Eunbyung Park. Deblurring 3d gaussian splatting. In *European Conference on Computer Vision*, pages 127–143. Springer, 2024. 2
- [21] Dogyoon Lee, Minhyeok Lee, Chajin Shin, and Sangyoun Lee. Dp-nerf: Deblurred neural radiance field with physical scene priors. In *Proceedings of the IEEE/CVF Conference on Computer Vision and Pattern Recognition (CVPR)*, pages 12386–12396, 2023. 2
- [22] Dongwoo Lee, Jeongtaek Oh, Jaesung Rim, Sunghyun Cho, and Kyoung Mu Lee. Exblurf: Efficient radiance fields for extreme motion blurred images. 2023. 1
- [23] Jungho Lee, Dogyoon Lee, Minhyeok Lee, Donghyung Kim, and Sangyoun Lee. Smurf: Continuous dynamics for motion-deblurring radiance fields. *arXiv preprint arXiv:2403.07547*, 2024. 2
- [24] Zhan Li, Zhang Chen, Zhong Li, and Yi Xu. Spacetime gaussian feature splatting for real-time dynamic view synthesis. In *Proceedings of the IEEE/CVF Conference on Computer Vision and Pattern Recognition*, pages 8508–8520, 2024. 2
- [25] Peidong Liu, Xingxing Zuo, Viktor Larsson, and Marc Pollefeys. Mba-vo: Motion blur aware visual odometry. *2021 IEEE/CVF International Conference on Computer Vision (ICCV)*, pages 5530–5539, 2021. 5
- [26] Yiren Lu, Jing Ma, and Yu Yin. View-consistent object removal in radiance fields. In *Proceedings of the 32nd ACM*

- International Conference on Multimedia*, pages 3597–3606, 2024. 1
- [27] Zhicheng Lu, Xiang Guo, Le Hui, Tianrui Chen, Min Yang, Xiao Tang, Feng Zhu, and Yuchao Dai. 3d geometry-aware deformable gaussian splatting for dynamic view synthesis. In *Proceedings of the IEEE/CVF Conference on Computer Vision and Pattern Recognition*, pages 8900–8910, 2024. 1, 2
- [28] Jonathon Luiten, Georgios Kopanas, Bastian Leibe, and Deva Ramanan. Dynamic 3d gaussians: Tracking by persistent dynamic view synthesis. In *3DV*, 2024. 2
- [29] Li Ma, Xiaoyu Li, Jing Liao, Qi Zhang, Xuan Wang, Jue Wang, and Pedro V. Sander. Deblur-nerf: Neural radiance fields from blurry images, 2021. 1, 2, 3, 5
- [30] Li Ma, Xiaoyu Li, Jing Liao, Qi Zhang, Xuan Wang, Jue Wang, and Pedro V Sander. Deblur-nerf: Neural radiance fields from blurry images. In *Proceedings of the IEEE/CVF Conference on Computer Vision and Pattern Recognition*, pages 12861–12870, 2022. 1, 2
- [31] Hidenobu Matsuki, Riku Murai, Paul H. J. Kelly, and Andrew J. Davison. Gaussian Splatting SLAM. In *Proceedings of the IEEE/CVF Conference on Computer Vision and Pattern Recognition*, 2024. 1
- [32] Ben Mildenhall, Pratul P. Srinivasan, Matthew Tancik, Jonathan T. Barron, Ravi Ramamoorthi, and Ren Ng. Nerf: Representing scenes as neural radiance fields for view synthesis. In *ECCV*, 2020. 1
- [33] Keunhong Park, Utkarsh Sinha, Peter Hedman, Jonathan T. Barron, Sofien Bouaziz, Dan B Goldman, Ricardo Martin-Brualla, and Steven M. Seitz. Hypernerf: A higher-dimensional representation for topologically varying neural radiance fields. *ACM Trans. Graph.*, 40(6), 2021. 5, 6, 1, 2
- [34] Cheng Peng and Rama Chellappa. Pdrf: Progressively deblurring radiance field for fast and robust scene reconstruction from blurry images. *arXiv preprint arXiv:2208.08049*, 2022. 2
- [35] Cheng Peng, Yutao Tang, Yifan Zhou, Nengyu Wang, Xijun Liu, Deming Li, and Rama Chellappa. Bags: Blur agnostic gaussian splatting through multi-scale kernel modeling. In *European Conference on Computer Vision*, pages 293–310. Springer, 2024. 2
- [36] Antoni Rosinol, John J Leonard, and Luca Carlone. Nerf-slam: Real-time dense monocular slam with neural radiance fields. In *2023 IEEE/RSJ International Conference on Intelligent Robots and Systems (IROS)*, pages 3437–3444. IEEE, 2023. 1
- [37] Johannes Lutz Schönberger and Jan-Michael Frahm. Structure-from-motion revisited. In *Conference on Computer Vision and Pattern Recognition (CVPR)*, 2016. 4
- [38] Johannes Lutz Schönberger, Enliang Zheng, Marc Pollefeys, and Jan-Michael Frahm. Pixelwise view selection for unstructured multi-view stereo. In *European Conference on Computer Vision (ECCV)*, 2016. 4
- [39] Otto Seiskari, Jerry Ylilammi, Valtteri Kaatrasalo, Pekka Rantalankila, Matias Turkulainen, Juho Kannala, Esa Rahtu, and Arno Solin. Gaussian splatting on the move: Blur and rolling shutter compensation for natural camera motion. In *European Conference on Computer Vision*, pages 160–177. Springer, 2024. 2
- [40] Joan Sola, Jeremie Deray, and Dinesh Atchuthan. A micro lie theory for state estimation in robotics. *arXiv preprint arXiv:1812.01537*, 2018. 4
- [41] Edgar Sucar, Shikun Liu, Joseph Ortiz, and Andrew Davison. iMAP: Implicit mapping and positioning in real-time. In *Proceedings of the International Conference on Computer Vision (ICCV)*, 2021. 1
- [42] Huiqiang Sun, Xingyi Li, Liao Shen, Xinyi Ye, Ke Xian, and Zhiguo Cao. Dyblurf: Dynamic neural radiance fields from blurry monocular video. In *Proceedings of the IEEE/CVF Conference on Computer Vision and Pattern Recognition*, pages 7517–7527, 2024. 1, 3, 6
- [43] Fu-Jen Tsai, Yan-Tsung Peng, Yen-Yu Lin, Chung-Chi Tsai, and Chia-Wen Lin. Stripformer: Strip transformer for fast image deblurring. In *European conference on computer vision*, pages 146–162. Springer, 2022. 2
- [44] Can Wang, Menglei Chai, Mingming He, Dongdong Chen, and Jing Liao. Clip-nerf: Text-and-image driven manipulation of neural radiance fields. In *Proceedings of the IEEE/CVF conference on computer vision and pattern recognition*, pages 3835–3844, 2022. 1
- [45] Chen Wang, Dasong Gao, Kuan Xu, Junyi Geng, Yaoyu Hu, Yuheng Qiu, Bowen Li, Fan Yang, Brady Moon, Abhinav Pandey, Aryan, Jiahe Xu, Tianhao Wu, Haonan He, Daning Huang, Zhongqiang Ren, Shibo Zhao, Taimeng Fu, Pranay Reddy, Xiao Lin, Wenshan Wang, Jingnan Shi, Rajat Talak, Kun Cao, Yi Du, Han Wang, Huai Yu, Shanzhao Wang, Siyu Chen, Ananth Kashyap, Rohan Bandaru, Karthik Dantu, Jijun Wu, Lihua Xie, Luca Carlone, Marco Hutter, and Sebastian Scherer. PyPose: A library for robot learning with physics-based optimization. In *IEEE/CVF Conference on Computer Vision and Pattern Recognition (CVPR)*, 2023. 4
- [46] Junjie Wang, Jiemin Fang, Xiaopeng Zhang, Lingxi Xie, and Qi Tian. Gaussianeditor: Editing 3d gaussians delicately with text instructions. In *Proceedings of the IEEE/CVF conference on computer vision and pattern recognition*, pages 20902–20911, 2024. 1
- [47] Peng Wang, Lingzhe Zhao, Ruijie Ma, and Peidong Liu. BAD-NeRF: Bundle Adjusted Deblur Neural Radiance Fields. In *Proceedings of the IEEE/CVF Conference on Computer Vision and Pattern Recognition (CVPR)*, pages 4170–4179, 2023. 1, 2, 3
- [48] Qianqian Wang, Vickie Ye, Hang Gao, Jake Austin, Zhengqi Li, and Angjoo Kanazawa. Shape of motion: 4d reconstruction from a single video. *arXiv preprint arXiv:2407.13764*, 2024. 2
- [49] Zhou Wang, Alan C Bovik, Hamid R Sheikh, and Eero P Simoncelli. Image quality assessment: from error visibility to structural similarity. *IEEE transactions on image processing*, 13(4):600–612, 2004. 2
- [50] Chen Wenbo and Liu Ligang. Deblur-gs: 3d gaussian splatting from camera motion blurred images. *Proc. ACM Comput. Graph. Interact. Tech. (Proceedings of I3D 2024)*, 7(1), 2024. 1, 2, 3
- [51] Jinyu Yang, Mingqi Gao, Zhe Li, Shang Gao, Fangjing

- Wang, and Feng Zheng. Track anything: Segment anything meets videos, 2023. [4](#)
- [52] Lihe Yang, Bingyi Kang, Zilong Huang, Zhen Zhao, Xiaogang Xu, Jiashi Feng, and Hengshuang Zhao. Depth anything v2. *arXiv:2406.09414*, 2024. [5](#)
- [53] Ziyi Yang, Xinyu Gao, Wen Zhou, Shaohui Jiao, Yuqing Zhang, and Xiaogang Jin. Deformable 3d gaussians for high-fidelity monocular dynamic scene reconstruction. In *Proceedings of the IEEE/CVF Conference on Computer Vision and Pattern Recognition*, pages 20331–20341, 2024. [1](#), [2](#), [6](#)
- [54] Zeyu Yang, Hongye Yang, Zijie Pan, and Li Zhang. Real-time photorealistic dynamic scene representation and rendering with 4d gaussian splatting. In *International Conference on Learning Representations (ICLR)*, 2024. [1](#), [2](#), [6](#)
- [55] Yu Yin, Kamran Ghasedi, HsiangTao Wu, Jiaolong Yang, Xin Tong, and Yun Fu. Nerfinveter: High fidelity nerf-gan inversion for single-shot real image animation. In *Proceedings of the IEEE/CVF Conference on Computer Vision and Pattern Recognition*, pages 8539–8548, 2023. [1](#)
- [56] Syed Waqas Zamir, Aditya Arora, Salman Khan, Munawar Hayat, Fahad Shahbaz Khan, Ming-Hsuan Yang, and Ling Shao. Multi-stage progressive image restoration. In *CVPR*, 2021. [6](#)
- [57] Syed Waqas Zamir, Aditya Arora, Salman Khan, Munawar Hayat, Fahad Shahbaz Khan, and Ming-Hsuan Yang. Restormer: Efficient transformer for high-resolution image restoration. In *Proceedings of the IEEE/CVF conference on computer vision and pattern recognition*, pages 5728–5739, 2022. [2](#)
- [58] Zitong Zhan, Xiangfu Li, Qihang Li, Haonan He, Abhinav Pandey, Haitao Xiao, Yangmengfei Xu, Xiangyu Chen, Kuan Xu, Kun Cao, et al. Pypose v0. 6: The imperative programming interface for robotics. *arXiv preprint arXiv:2309.13035*, 2023. [4](#)
- [59] Hongguang Zhang, Yuchao Dai, Hongdong Li, and Piotr Koniusz. Deep stacked hierarchical multi-patch network for image deblurring. In *Proceedings of the IEEE/CVF conference on computer vision and pattern recognition*, pages 5978–5986, 2019. [2](#)
- [60] Richard Zhang, Phillip Isola, Alexei A Efros, Eli Shechtman, and Oliver Wang. The unreasonable effectiveness of deep features as a perceptual metric. In *Proceedings of the IEEE conference on computer vision and pattern recognition*, pages 586–595, 2018. [2](#)
- [61] Lingzhe Zhao, Peng Wang, and Peidong Liu. Bad-gaussians: Bundle adjusted deblur gaussian splatting. In *European Conference on Computer Vision (ECCV)*, 2024. [1](#), [2](#), [3](#), [4](#)
- [62] Shangchen Zhou, Jiawei Zhang, Wangmeng Zuo, Haozhe Xie, Jinshan Pan, and Jimmy Ren. Davanet: Stereo deblurring with view aggregation. In *CVPR*, 2019. [1](#), [2](#)
- [63] Ruijie Zhu, Yanzhe Liang, Hanzhi Chang, Jiacheng Deng, Jiahao Lu, Wenfei Yang, Tianzhu Zhang, and Yongdong Zhang. Motions: Exploring explicit motion guidance for deformable 3d gaussian splatting. *Advances in Neural Information Processing Systems*, 37:101790–101817, 2024. [1](#), [2](#)
- [64] Zihan Zhu, Songyou Peng, Viktor Larsson, Weiwei Xu, Hujun Bao, Zhaopeng Cui, Martin R. Oswald, and Marc Pollefeys. Nice-slam: Neural implicit scalable encoding for slam. In *Proceedings of the IEEE/CVF Conference on Computer Vision and Pattern Recognition (CVPR)*, 2022. [1](#)

BARD-GS: Blur-Aware Reconstruction of Dynamic Scenes via Gaussian Splatting

Supplementary Material

7. Real-world Motion Blur Dataset

Motion blur is a common occurrence in everyday photography, especially in dynamic scenes. Our proposed dataset addresses a crucial gap in existing resources by capturing realistic blurs caused by camera motion and fast-moving objects, making it highly relevant for studying real-world dynamic scene reconstruction. Table 5 compares the key characteristics across different datasets. While most datasets either lack blur entirely (e.g. HyperNeRF [33] and iPhone [10]) or rely on synthetic blur (e.g. Stereo Blur [62]), ours and Deblur-NeRF [30] are the only ones incorporating real-world blur. However, unlike Deblur-NeRF, which focuses on static scenes without object motion blur, our dataset offers a comprehensive and realistic benchmark for evaluating and developing solutions to complex motion blur challenges in dynamic settings.

7.1. Data Acquisition Process

We present the first real-world motion blur dataset specifically designed for dynamic scene reconstruction. The captured videos incorporate camera motions and fast-moving objects, which are typically encountered in real-world scenarios. Figure 7 illustrates sample frames from our dataset.

Our dataset is captured using two synchronized GoPro Hero 12 cameras. One camera is configured with a 1/24-second shutter speed to record 24 FPS *blurry* videos, while the other employs a 1/240-second shutter speed to capture 240 FPS *sharp* videos. The sharp videos are used for evaluation purposes only. To ensure precise synchronization, we utilized the timecode feature¹ provided by GoPro Lab firmware, complemented by manual timestamp alignment. This approach achieves a time offset of less than 1 millisecond, ensuring high temporal accuracy.

7.2. Data Pre-processing

Camera Pose Estimation. We begin by running COLMAP on all sharp images to obtain accurate camera poses, which serve as a reference for evaluation. Blurry images are then sequentially registered to this COLMAP reconstruction, producing intentionally inaccurate camera poses for training. This process aligns both sharp and blurry images within a unified world space, enabling precise evaluations. Additionally, the intentional inaccuracy of the blurry image camera poses mirrors real-world conditions, enhancing the realism of the training setup.

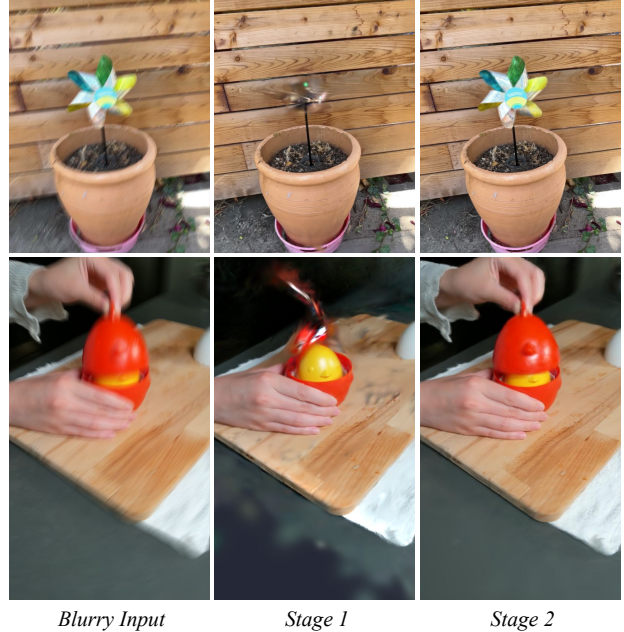


Figure 6. **Illustration of the two-stage training process.** The 2nd column shows outputs of *Stage 1*, where static regions are sharply reconstructed (e.g., the wooden background, flowerpot (top row), and cutting board (bottom row)). The 3rd column displays the outputs of *Stage 2*, where dynamic components, such as the spinning windmill (top row) and the lifting cap (bottom row), are clarified.

Point Cloud Initialization. Using these intentionally inaccurate camera poses, we perform a second reconstruction to generate an initial point cloud for training. Our method refines and optimizes the camera poses, resulting in final reconstructions that may exhibit slight shifts compared to those based on the unoptimized poses. Since other methods do not update poses, we ensure fair comparisons during evaluation by using shift-invariant metrics that tolerate minor pixel-level shifts in rendered images.

8. Two-Stage Training

Figure 6 illustrates the outputs at each stage of our proposed framework, which progressively refines the static and dynamic components within the scene.

In *stage 1*, we focus on mitigating camera motion blur by optimizing the camera trajectory, resulting in sharp reconstructions of static regions (e.g., the wooden background, floor, and flowerpot in the top-row example, and the table and cutting board in the bottom-row example). Since super-

¹<https://gopro.github.io/labs/control/precisiontime/>

Table 5. **Comparison of Dataset Characteristics.** Our dataset bridges a critical gap in current benchmarks by capturing real-world motion blur caused by both camera movement and fast-moving objects in dynamic scenes, providing a realistic and advanced resource for research.

Dataset	Dynamic Scene	Blur Type	Blur Cause		# Cameras	# Scenes	Frame Rate (FPS)
			Camera Motion	Object Motion			
HyperNeRF [33]	✓	×	×	×	2	17	15
iPhone [10]	✓	×	×	×	3	14	30 / 60
Deblur-NeRF [30]	×	Real-World	✓	×	1	30	–
Stereo Blur [62]	✓	Synthetic	✓	Slow	2	135	60
Ours	✓	Real-World	✓	Fast	2	12	24 / 240

vision is limited to the static regions during this stage, the reconstructions of dynamic regions remain incomplete and exhibit random artifacts.

In *stage 2*, we address object motion blur by modeling object movements using Gaussian motion trajectories. This stage allows for clearer reconstruction of dynamic regions, such as the spinning windmill in the top row and the cap being lifted in the bottom row. Simultaneously, static details are further refined through the introduction of a deformation field for static Gaussians, ensuring the overall enhancement of scene details.

phasize the importance of each component in our method for achieving clear, artifact-free results.

9. Additional Results of Novel View Synthesis

To further demonstrate the effectiveness of our proposed method, we show additional comparison results for novel view synthesis in Figure 8 and 9. Each scene includes four distinct novel views, with dynamic regions highlighted by dashed yellow boxes and static regions by green boxes. Our method consistently outperforms baseline approaches, delivering superior reconstruction quality in both static and dynamic regions.

Additionally, quantitative comparisons of novel view synthesis across 7 captured scenes in our dataset are provided in Table 6. We report the results of five metrics, including shift-invariant PSNR (SI-PSNR), shift-invariant SSIM [49] (SI-SSIM), shift-invariant LPIPS [60] (SI-LPIPS), Laplacian Variance score (LV) [2], and MUSIQ [14]. Our approach achieves the best performance for the majority of scenes across all five metrics, underscoring its robustness and effectiveness.

10. Ablation Study of Proposed Components

In this section, we illustrate the impact of each component on the final reconstruction quality, as shown in Figure 10. We can see that removing either tracking loss (*w/o TL*) or object motion deblurring (*w/o DB*) results in significant blurring of dynamic regions. Omitting static deblurring (*w/o SD*) causes blurring in the static regions, while the exclusion of static deformation field (*w/o SDF*) introduces floating artifacts in the static regions, leading to occlusions and distortions in the dynamic regions. These results em-

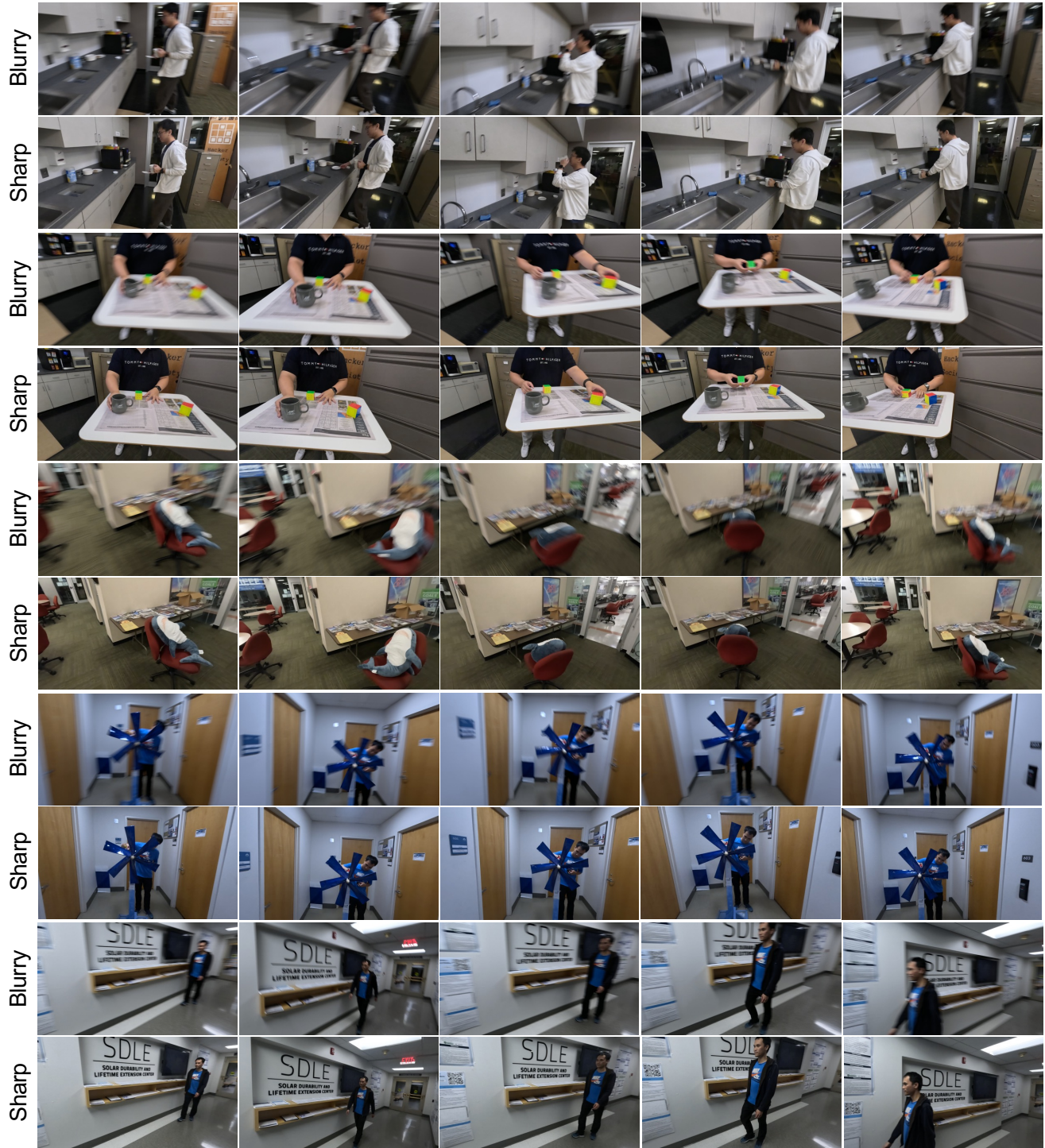


Figure 7. **Samples from our real-world blurry dataset.** Each row pair showcases blurry input frames (top of each pair) alongside their corresponding sharp ground-truth frames (bottom of each pair). The dataset captures diverse scenarios with fast-moving objects and camera motion, reflecting real-world challenges.

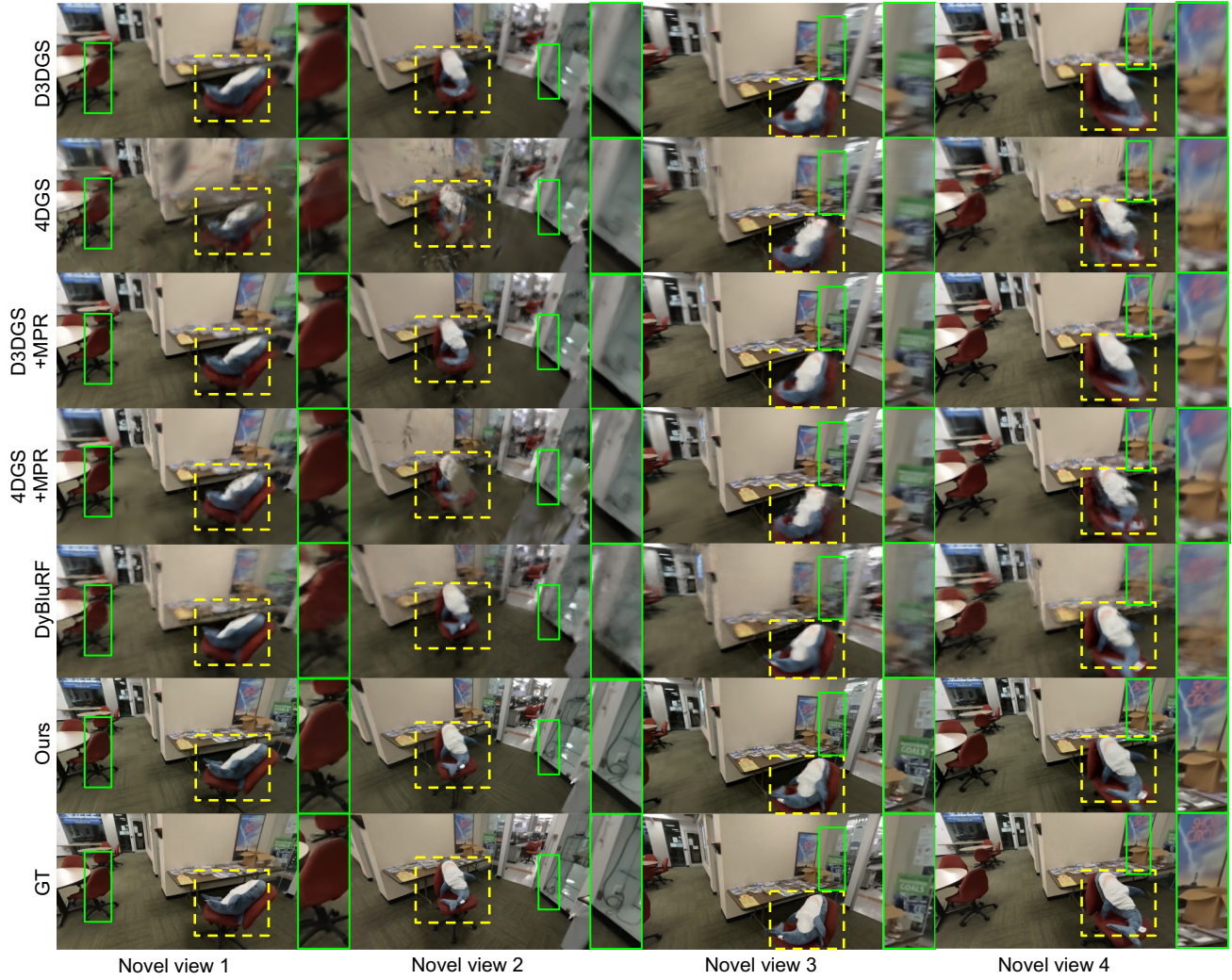


Figure 8. **Novel view comparison on the “shark-spin” scene.** Green boxes highlight details in static regions, while the dashed yellow boxes indicate dynamic areas. Our method demonstrates significantly better reconstruction in the dynamic region (*i.e.*, the shark toy on the spinning chair) and preserves superior details in static regions (*e.g.*, the red chair in the background, wires in the back, and posters on the wall) across all novel views.

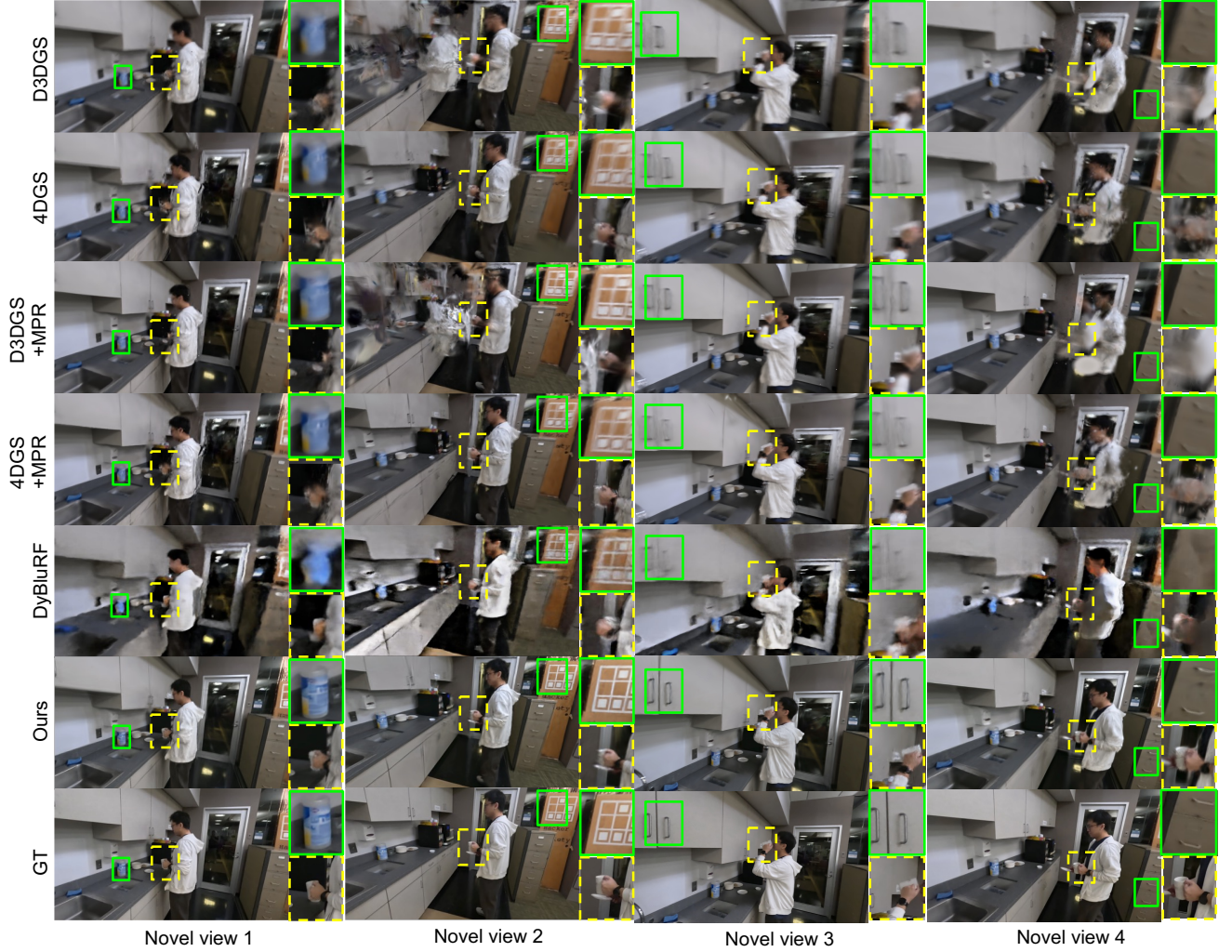


Figure 9. **Novel view comparison on the “kitchen” scene.** Green boxes highlight fine details in static regions, and the dashed yellow boxes indicate dynamic parts. Our method demonstrates superior reconstruction in static regions, accurately capturing intricate elements such as the cleaning bottle, wall painting, and cabinet handles. Additionally, it effectively mitigates blur caused by moving objects, such as the moving hand and body. These results emphasize our method’s ability to preserve detailed textures and address challenging visual artifacts in both static and dynamic regions.

Table 6. **Quantitative novel view synthesis comparison across 7 captured scenes in our dataset.** The results are evaluated using five metrics: SI-PSNR (\uparrow), SI-SSIM (\uparrow), SI-LPIPS (\downarrow), LV (\uparrow), and MUSIQ (\uparrow). Colors indicate the **best** and **second best** results, respectively. Our approach achieves the best results across all scenes for all five metrics in most cases.

	card					toycar					windmill				
	SI-PSNR \uparrow	SI-SSIM \uparrow	SI-LPIPS \downarrow	LV \uparrow	MUSIQ \uparrow	SI-PSNR \uparrow	SI-SSIM \uparrow	SI-LPIPS \downarrow	LV \uparrow	MUSIQ \uparrow	SI-PSNR \uparrow	SI-SSIM \uparrow	SI-LPIPS \downarrow	LV \uparrow	MUSIQ \uparrow
DyBluRF	19.86	0.7602	0.4102	13.75	35.11	18.15	0.7912	0.3303	41.68	36.96	21.79	0.7932	0.2630	14.94	33.32
D3DGS	23.97	0.8323	0.3111	19.45	37.02	20.58	0.8588	0.2811	29.51	43.33	20.32	0.8014	0.4696	8.06	25.25
D3DGS+MPR	24.09	0.8323	0.2226	59.69	50.54	20.06	0.8529	0.3213	37.12	43.53	22.63	0.8632	0.2401	15.37	34.21
4DGS	22.33	0.8290	0.3323	38.46	40.09	20.84	0.8519	0.2935	35.72	43.75	21.37	0.8236	0.4022	8.76	24.47
4DGS+MPR	22.58	0.8459	0.2809	76.38	54.29	20.94	0.8621	0.2513	74.51	55.07	23.29	0.8575	0.2855	20.10	36.40
Ours	25.76	0.8332	0.1701	78.29	63.38	23.47	0.8676	0.1419	60.04	57.17	27.52	0.9063	0.1275	69.11	48.44
	shark-spin					walk					kitchen				
	SI-PSNR \uparrow	SI-SSIM \uparrow	SI-LPIPS \downarrow	LV \uparrow	MUSIQ \uparrow	SI-PSNR \uparrow	SI-SSIM \uparrow	SI-LPIPS \downarrow	LV \uparrow	MUSIQ \uparrow	SI-PSNR \uparrow	SI-SSIM \uparrow	SI-LPIPS \downarrow	LV \uparrow	MUSIQ \uparrow
DyBluRF	22.59	0.7816	0.4099	11.39	18.14	19.34	0.7301	0.2732	123.51	40.30	18.76	0.7004	0.4311	27.83	23.71
D3DGS	24.09	0.8192	0.3814	11.43	19.77	21.99	0.7880	0.3067	31.81	24.76	22.87	0.8223	0.3798	10.89	23.85
D3DGS+MPR	24.06	0.8369	0.3156	17.73	28.74	21.68	0.7965	0.2165	80.01	41.22	22.94	0.8424	0.2690	18.26	31.21
4DGS	21.23	0.7676	0.4922	12.16	21.39	20.94	0.7641	0.3247	47.37	27.59	22.66	0.8109	0.3523	14.44	24.64
4DGS+MPR	22.33	0.8011	0.3739	23.16	28.86	20.79	0.773	0.2529	100.26	45.51	22.81	0.8325	0.2460	27.35	31.34
Ours	25.43	0.8562	0.1575	96.45	49.88	23.31	0.8268	0.1440	216.54	52.05	23.47	0.8326	0.1670	68.84	45.32
	poster					average									
	SI-PSNR \uparrow	SI-SSIM \uparrow	SI-LPIPS \downarrow	LV \uparrow	MUSIQ \uparrow	SI-PSNR \uparrow	SI-SSIM \uparrow	SI-LPIPS \downarrow	LV \uparrow	MUSIQ \uparrow					
DyBluRF	23.51	0.7803	0.4199	13.03	29.84	20.57	0.7614	0.3614	35.16	31.05					
D3DGS	25.99	0.8396	0.3280	21.50	28.25	22.83	0.8243	0.3500	18.95	28.89					
D3DGS+MPR	26.22	0.8302	0.2607	34.87	41.64	23.10	0.8363	0.2637	37.58	38.73					
4DGS	24.99	0.8177	0.4160	15.27	29.25	22.06	0.8093	0.3733	24.60	30.17					
4DGS+MPR	25.30	0.8332	0.3135	32.93	41.63	22.58	0.8293	0.2863	50.68	41.88					
Ours	26.96	0.8360	0.1890	85.68	63.82	25.13	0.8508	0.1567	96.42	54.29					

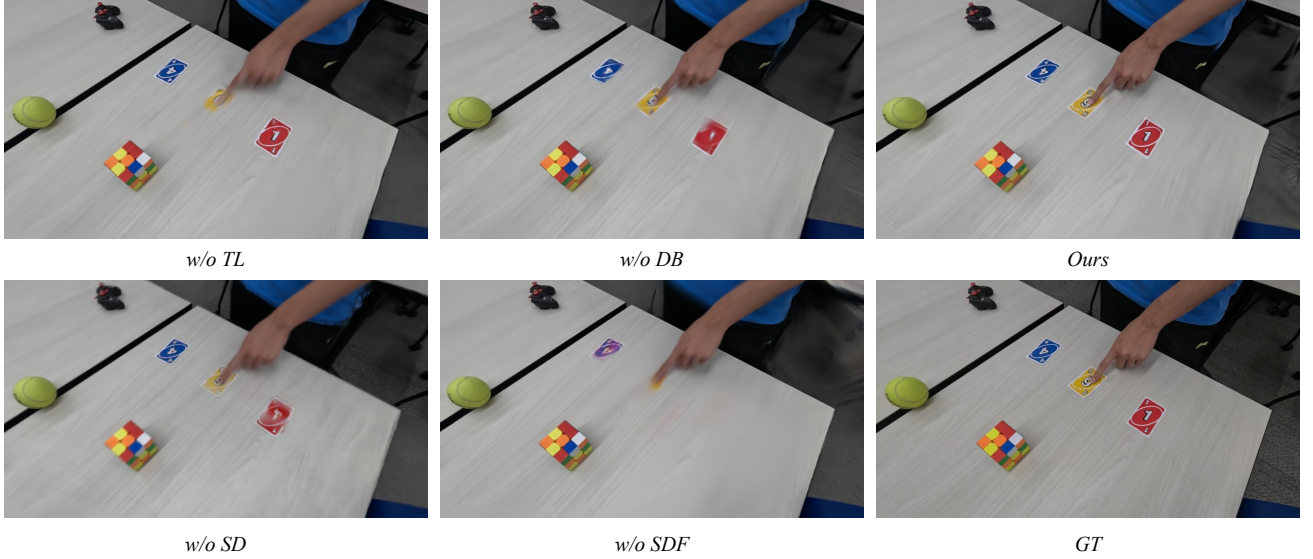


Figure 10. **Visual comparison of component ablation study.** *w/o TL* denotes the exclusion of tracking loss (\mathcal{L}_{track}), while *w/o DB* indicates the removal of *stage 2: Dynamic region deBlurring*. Similarly, *w/o SD* refers to the absence of *stage 1: Static region Deblurring*, and *w/o SDF* signifies the exclusion of *Static Deformation Field* in *stage 2*. These comparisons highlight the critical contributions of each component of the proposed approach to achieving clear and artifact-free results.